Electronic Supplementary Material (ESI) for Chemical Science.

Degradation and regeneration of Fe-N$_x$ active sites for oxygen reduction reaction: the role of surface oxidation, Fe demetallation and local carbon microporosity

Dongsheng Xia,[a] Chenchen Yu,[a] Yinghao Zhao,[a] Yinping Wei,[a] Haiyan Wu,[a] Yongqiang Kang,[a] Jia Li,[a], [b],* Lin Gan,[a],* Feiyu Kang[a], [b], *

Email: li.jia@sz.tsinghua.edu.cn, lgan@sz.tsinghua.edu.cn, fykang@mail.tsinghua.edu.cn

[a]Institute of Materials Research and Shenzhen Geim Graphene Research Center, Tsinghua Shenzhen International Graduate School, Tsinghua University, Shenzhen 518055, P. R. China

[b]Guangdong Provincial Key Laboratory of Thermal Management Engineering and Materials, Tsinghua Shenzhen International Graduate School, Tsinghua University, Shenzhen 518055, P. R. China

EXPERIMENTAL SECTION

Preparation of Catalysts. The FeNC900 catalyst was first synthesized by carbonizing the Fe-doped zeolitic imidazolate frameworks-8 (Fe-ZIF-8) precursor under argon (Ar) atmosphere at 900 ℃ for 3 h (heating ramp 5 ℃ min^{-1}). The detailed synthesis procedures of the Fe-ZIF-8 precursor were reported in our latest work, where the related catalyst was marked as Fe-ZIF'.[1] Typically, 657 mg 2-methylimidazole (8 mmol) was first dissolved with 15 mL methanol in beaker Ⅰ, and 605 mg zinc nitrate hexahydrate (2 mmol) and 70 mg iron (Ⅲ) acetylacetonate (0.2 mmol) were dissolved with 30 mL methanol in beaker Ⅱ. Then the two solutions were mixed with continuous stirring for 1h, and the obtained solution was finally subjected to solvothermal reaction at 120 °C for 4 h in a stainless reactor (with a Teflon liner). The obtained product was fully washed with DMF (3 times) and methanol (3 times) to remove the red Fe-containing ionomer as much as possible, and dried in an oven under vacuum at 60 ℃ for over 10 h, thus obtaining the Fe-ZIF-8 precursor. The FeNC900-HP catalyst was subsequently prepared by chemically treating the FeNC900 catalyst in H_2O_2-containing 0.1 M $HClO_4$ solution. Specifically, 100 mg FeNC900 catalyst was carefully added into 135 mL 3wt% H_2O_2-containing 0.1 M $HClO_4$ (1.35 mol H_2O_2 per gram of catalyst) with continuous stirring at room temperature for 12 h. After that, the treated catalyst was filtered and washed with ultrapure water, then dried in a vacuum oven (60 ℃, > 10 h), thus obtaining the FeNC900-HP catalyst. Then, the FeNC900-HP-600 and FeNC900-HP-900 catalysts were prepared by post thermal annealing of the FeNC900-HP catalyst at 600 and 900 ℃, respectively, for 2 h under Ar atmosphere (heating ramp 10 ℃ min^{-}

^{1}). The FeNC900-HP-900A catalyst was finally obtained via subsequent ammonolysis (5% NH_3 + 95% Ar at 900 ℃ for 10 min) of the FeNC900-HP-900 catalyst.

Physical Characterization. Pore structures were analyzed by N_2 physisorption measurement at 77 K using an ASAP 2020M+C equipment, where the specific surface area was calculated based on Brunauer-Emmett-Teller (BET) model, and mesopore- and micropore-size distributions were analyzed employing the Barrett-Joyner-Halenda (BJH) and Horvath-Kawazoe (HK) models, respectively. The micropore/external surface areas of the as-synthesized catalysts were analyzed based on their respective *t*-plots. Phase compositions were identified by X-ray diffraction (XRD) on a D8 Advance machine using the monochromatic Cu K_α X-ray source. X-ray photoelectron spectroscopy (XPS) tests were conducted on PHI5000VersaProbeII (Thermo Fisher) equipment using the monochromatic Al K_α X-ray source, to probe the chemical states of elements of interest within the near-surface region of the studied catalysts. Transmission electron microscopy (TEM), selected area electron diffraction (SAED) and elemental mapping *via* electron energy loss spectroscopy (EELS, with STEM mode) were performed on an FEI Tecnai G2 F30 TEM equipped with a Gatan Image Filter 965ER system. Aberration-corrected annular-dark-field scanning transmission electron microscopy (ADF-STEM) images were recorded to distinguish Fe single atoms on carbon matrix. Inductively coupled plasma-mass spectroscopy (ICP-MS) analysis were carried out to identify whether the acidic H_2O_2 treatment could lead to the demetallation of Fe-N_x moieties. To improve the accuracy of the ICP-MS results, the FeNC900 catalyst was fully acid-leached before the ICP-MS analysis to remove any possible exposed Fe/Fe_3C nanoparticles; the acid-leached product was subsequently oxidized into Fe oxides in the air and then acid digested for the ICP-MS analysis. ^{57}Fe Mossbauer spectra were measured at room temperature with a source of ^{57}Co. The velocity calibration was performed with an α-Fe foil.

Electrochemical Characterization. All electrochemical tests were carried out on a potentiostat coupled with a rotating disk electrode (RDE, disk diameter 5 mm) as the working electrode. H-type three-compartment cell physically separated by porous ceramics was used in this work to avoid the potential effects of the counter electrode on the electrochemical evaluation of the working electrode.[2] Using the H-type cell, the same catalyst film on RDE showed the same ORR polarization characteristics regardless of the counter electrode (Pt wire vs. graphitic rod) employed (Fig. S1). In this work, graphitic rod was used as counter electrode in most electrochemical tests. Hg/Hg_2SO_4@saturated K_2SO_4(aq) (MMS) electrode was chosen as the reference electrode. Before electrochemical tests, the potential of the reference MMS electrode was calibrated on the scale of the reversible hydrogen electrode (RHE) in H_2-saturated 0.1 M $HClO_4$ electrolyte. The ORR activities of the as-prepared catalysts were evaluated in 0.1 M $HClO_4$ electrolyte by two protocols: linear sweep polarization curves (potential scan rate: 5 mV s^{-1}) and steady-state polarization curves. For the linear sweep voltammetry tests, all measured ORR currents were corrected by capacitance currents obtained in the N_2-saturated electrolyte and all potentials were compensated by the Ohomic drop (iR), where R is the electrolyte resistance between the working electrode and the reference electrode. The steady-state polarization curves were recorded using discrete potential steps of 50 mV at intervals of 30 s from 0 V to 1.0 V vs. RHE. The kinetic current density was calculated according to the Koutechy-Levich equation:

$$j^{-1} = j_{\mathrm{d}}^{-1} + j_{\mathrm{k}}^{-1}$$

where j, j_{d}, and j_{k} denote the measured ORR current density, diffusion-limited current density, and kinetic current density, respectively. A rotating ring-disk electrode (RRDE, disk diameter 5.61 mm) was used to evaluate the H_2O_2 yield, where the ring potential was set at 1.3 V/RHE. The catalyst loading and electrode rotation speed were set at ca. 0.4 mg cm^{-2} and 1600 r.p.m., respectively. In situ electrochemical quantification of the active Fe-N_x sites was conducted by NO_2^--stripping voltammetry method proposed by Malko et al.[3] Briefly, extensive potential cycling in pH 5.2 acetate buffer electrolyte was first performed in alternative N_2 and O_2 (-0.4~1.05 V/RHE) to guarantee a non-changing CV in N_2. Before poisoned by $NaNO_2$, a CV curve (0.4~-0.3 V/RHE) was first recorded as the baseline, then the catalyst was poisoned by $NaNO_2$, and another CV curve (also 0.4~-0.3 V/RHE) was subsequently recorded, during which the adsorbed NO_2^- on the central Fe ion could be reduced via a five-electron pathway. The excessive part of the NO_2^--stripping CV curve compared to the CV baseline represents the reduction charge of NO_2^-, which was proportional to the site density. The site density (SD) and mean TOF can be respectively calculated according to the following formulas:[4]

$$\mathrm{SD}\ (\mathrm{mol\ g^{-1}}) = \frac{Q_{\mathrm{strip}}\ (\mathrm{C\ g^{-1}})}{n_{\mathrm{strip}}\, F\ (\mathrm{C\ mol^{-1}})} \qquad (1)$$

$$\mathrm{TOF}\ (\mathrm{s}^{-1}) = \frac{n_{\mathrm{strip}}\ \Delta j_{\mathrm{k}}(\mathrm{mA\ cm}^{-2})}{Q_{\mathrm{strip}}\ (\mathrm{C\ g}^{-1})\ L_{\mathrm{cat.}}(\mathrm{mg\ cm}^{-2})} \tag{2}$$

where Q_{strip} and n_{strip} (= 5) represent the reduction charge of NO_2^- and the corresponding electron transfer number, respectively; j_{k} is the kinetic current density and $L_{\mathrm{cat.}}$ the catalyst loading.

Theoretical calculations. All spin-polarized calculations were performed within the framework of density functional theory (DFT), as implemented in the Vienna *ab initio* Simulation Package (VASP).[5, 6] The projected augmented wave (PAW) potential was employed to describe the electron-ion interaction.[7] The exchange-correlation energy was described by using the Perdew-Burke-Ernzerhof (PBE) functional within generalized gradient approximation.[8] The plane wave cutoff energy was adopted as 520 eV. Gaussian smearing of 0.05 eV was applied to the orbital occupation during the whole calculations. A 20-Å-thick vacuum layer was used to eliminate the spurious interaction between adjacent graphene layers along the *z*-direction. All atoms were allowed to fully relax by the conjugate gradient (CG) algorithm until the force on each atom was less than 0.01 eV/Å. A Γ-centered $2 \times 2 \times 1$ *k*-grid and $4 \times 4 \times 1$ *k*-grid were used to sample the Brillouin zone of supercell for geometry optimization and electronic structure calculations, respectively. The ORR activity was calculated under the theoretical framework developed by Nørskov et al.[9] Crystal orbital Hamilton population (COHP) analysis was performed by using LOBSTER code.[10, 11]

Table S1 Mössbauer parameters for iron sites as found in the FeNC900 catalyst.

	IS (mm s^{-1})	ΔE_Q (mm s^{-1})	Relative area (%)	Assignment
D1	0.34	0.88±0.01	53.7	$Fe(III)N_4C_{12}$, HS
D2	0.16±0.02	2.37±0.06	38.3	$Fe(II)N_4C_{10}$, LS/MS
D3	0.97±0.04	2.68±0.09	8.1	$Fe(II)N_4/C$, HS

FIGURES

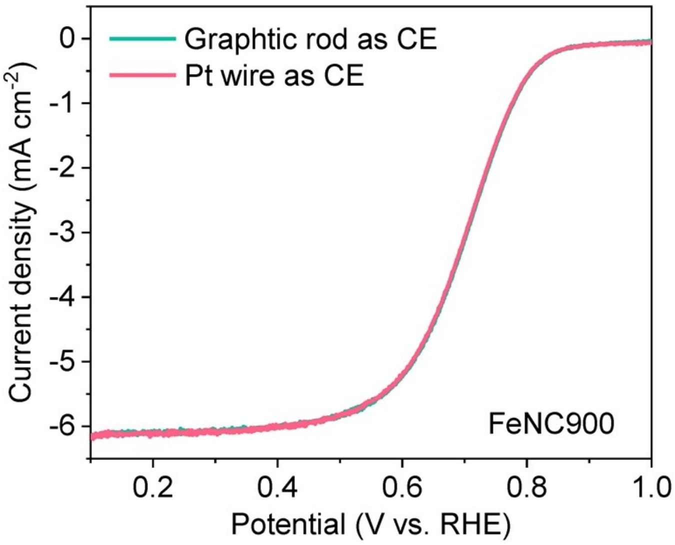

Figure S1. The effect of counter electrode (CE) on the polarization curve evaluation performed in a H-type two-compartment cell. As can be seen, the same catalyst film on RDE showed the same ORR polarization characteristics regardless of the counter electrode (Pt wire vs. graphitic rod) employed.

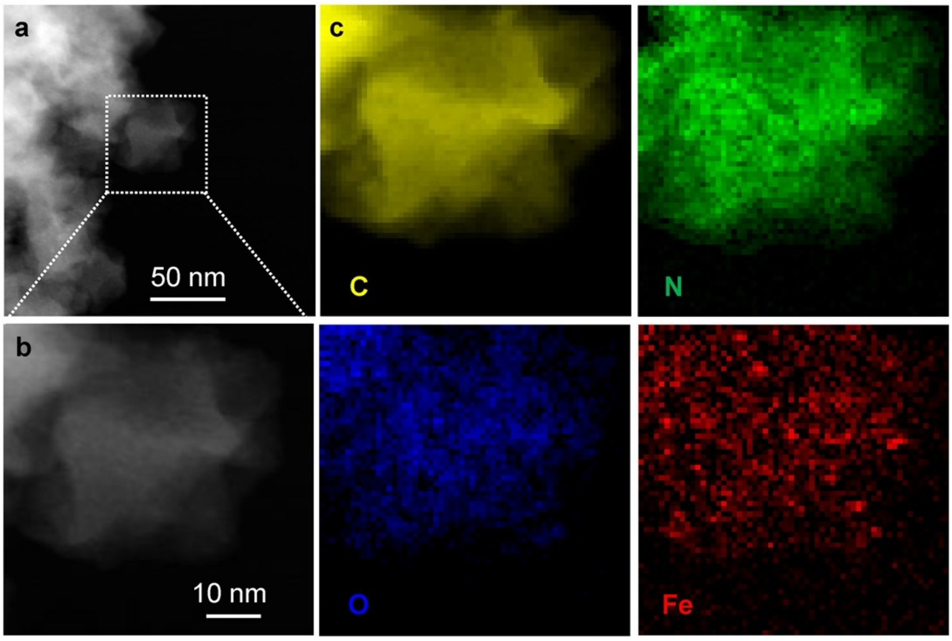

Figure S2. Annular dark field STEM characterization for the FeNC900 catalyst. (a) STEM image under low magnification. (b) STEM image under high magnification. (c) Elemental mapping results based on the corresponding STEM EELS data.

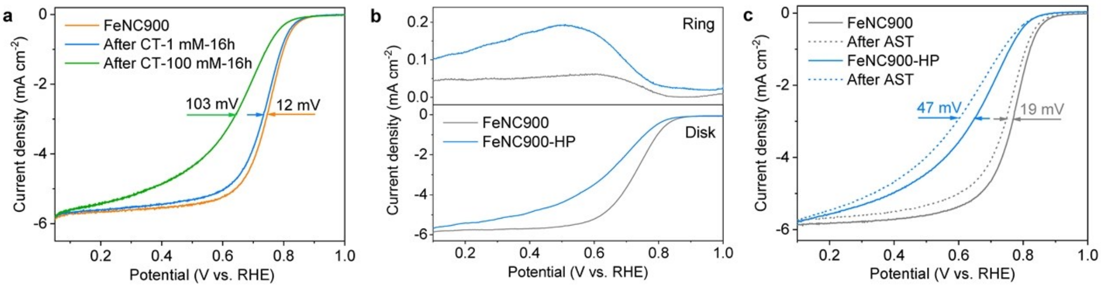

Figure S3. (a) Stability evaluation of the FeNC900 catalyst by chemical treatment (CT) of H_2O_2, where the FeNC900 catalyst-coated RDE electrode was soaked in 0.1 M $HClO_4$ electrolyte (80 mL) with different H_2O_2 concentration for 16h. (b) H_2O_2 yield evaluation for both the FeNC900 and FeNC900-HP catalysts by RRDE technique, the ring potential was set at 1.3 V/RHE. (c) Stability evaluation of both the FeNC900 and FeNC900-HP catalysts in O_2-saturated 0.1 M $HClO_4$ electrolyte. AST: 5000 potential cycles between 0.6~0.9 V/RHE at a scan rate of 50 mV s^{-1}.

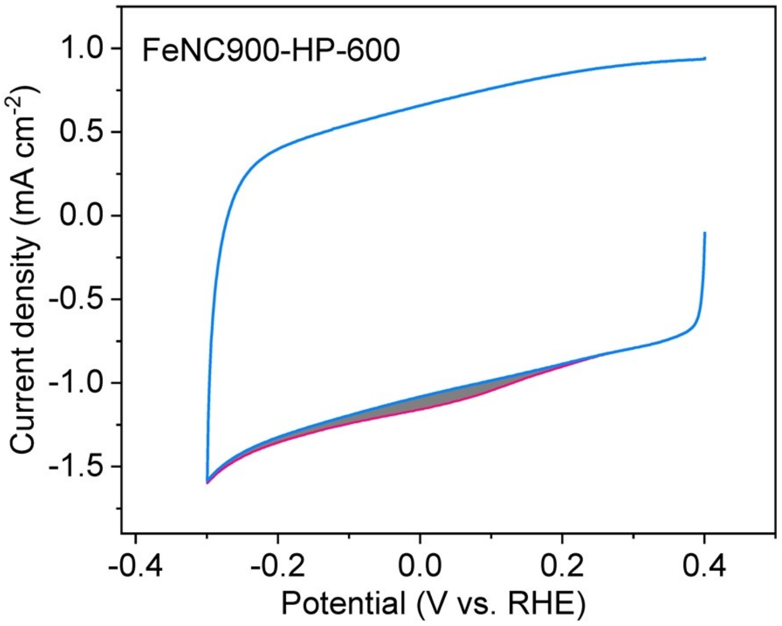

Figure S4. In-situ electrochemical NO_2^- stripping voltammetry for the FeNC900-HP-600 catalyst, where NO_2^- was used as a molecular probe in pH = 5.2 acetate buffer according to the work by Malko et al.[3]

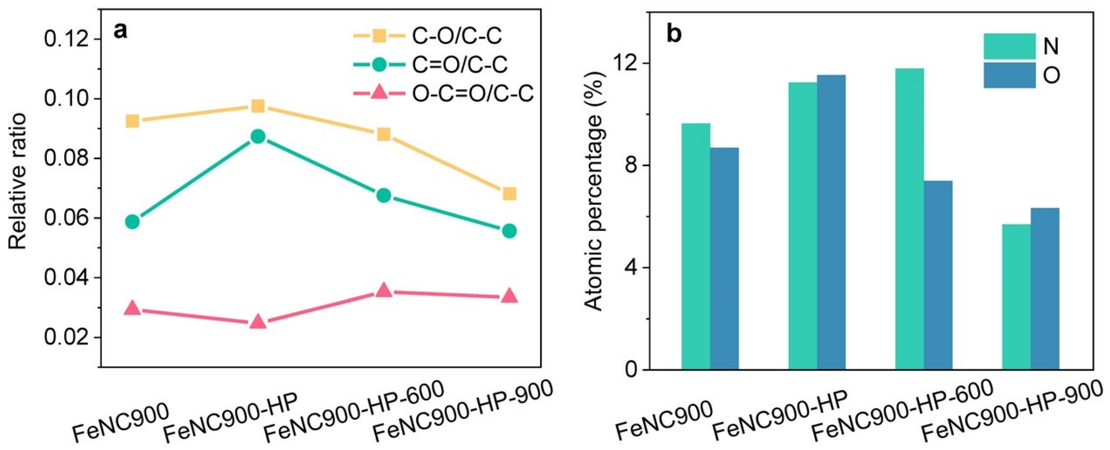

Figure S5. Quantification analysis of XPS data. (a) surface concentrations of different OFGs relative to C-C component. (b) total surface N and O contents.

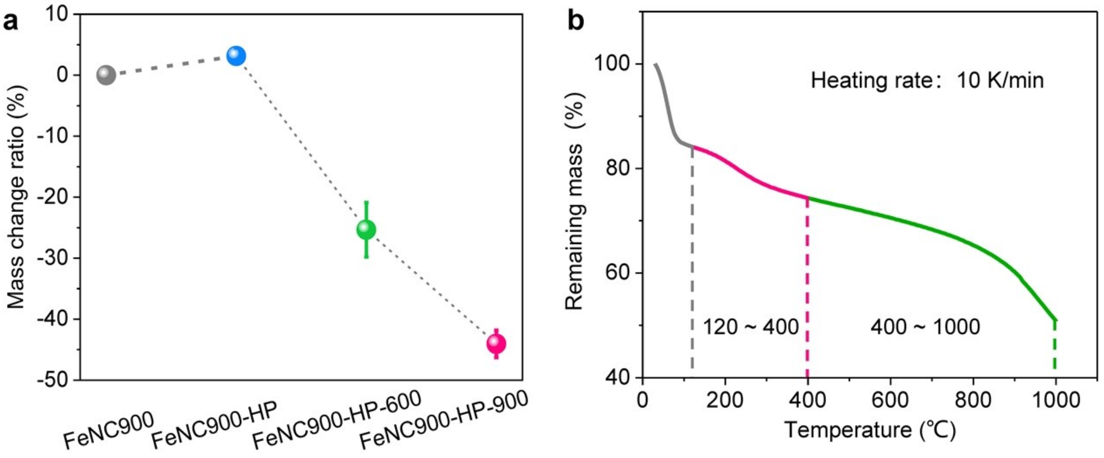

Figure S6. (a) Effect of post treatments on mass change normalized by the mass of the FeNC900 catalyst. (b) Thermogravimetric analysis of the FeNC900-HP catalyst under an Ar gas atmosphere.

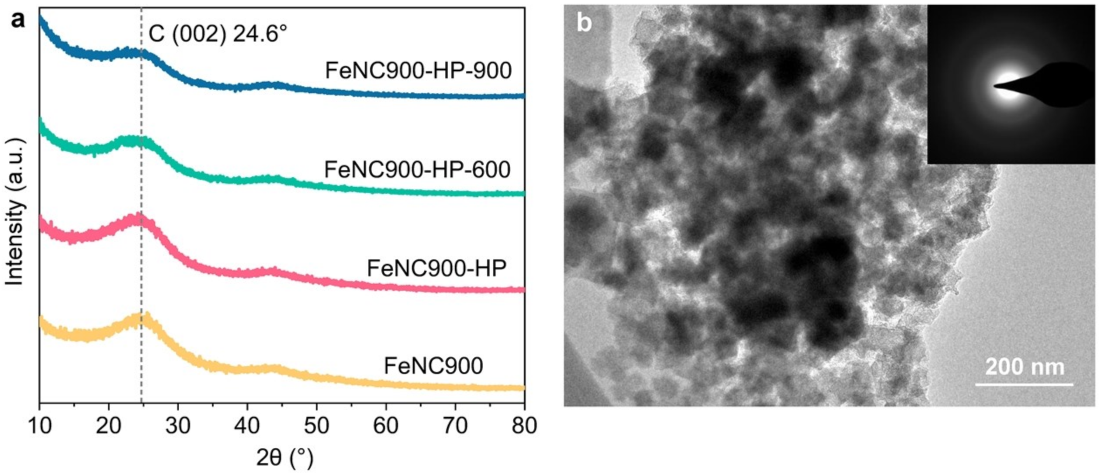

Figure S7. (a) XRD patterns of the as-prepared catalysts. No perceptible Fe-containing crystalline species (such as metal Fe and Fe_3C) are found, indicating Fe mainly exists in atomically dispersed Fe-N_x sites. (b) TEM image of the FeNC900-HP-900 catalyst, the inset of SAED pattern showing amorphous carbon structure without any diffraction signals of Fe-containing crystalline species, consistent with the corresponding XRD result.

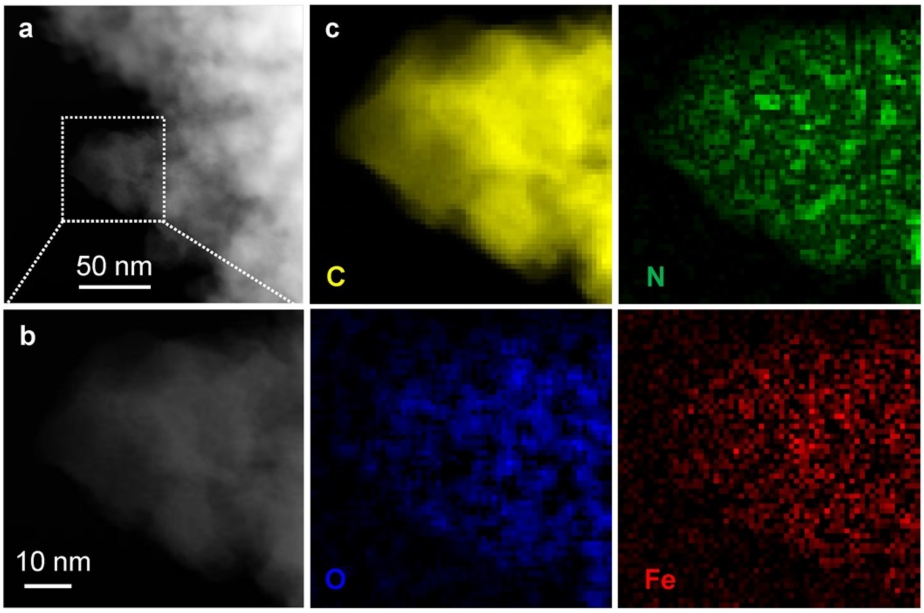

Figure S8. Annular dark field STEM characterization for the FeNC900-HP catalyst. (a) STEM image under low magnification. (b) STEM image under high magnification. (c) Elemental mapping results based on the corresponding STEM EELS data.

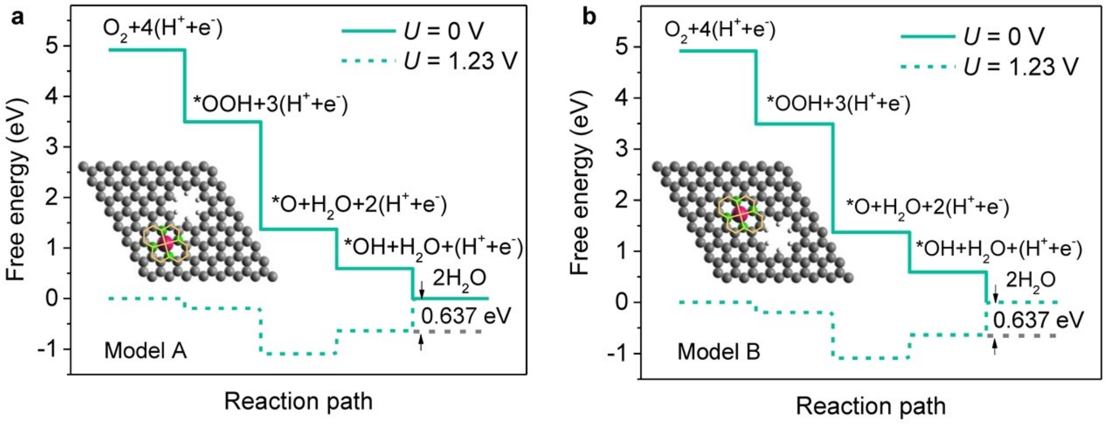

Figure S9. Free energy diagrams of model A (a) and model B (b) under zero potential (solid line) and the equilibrium potential (dashed line).

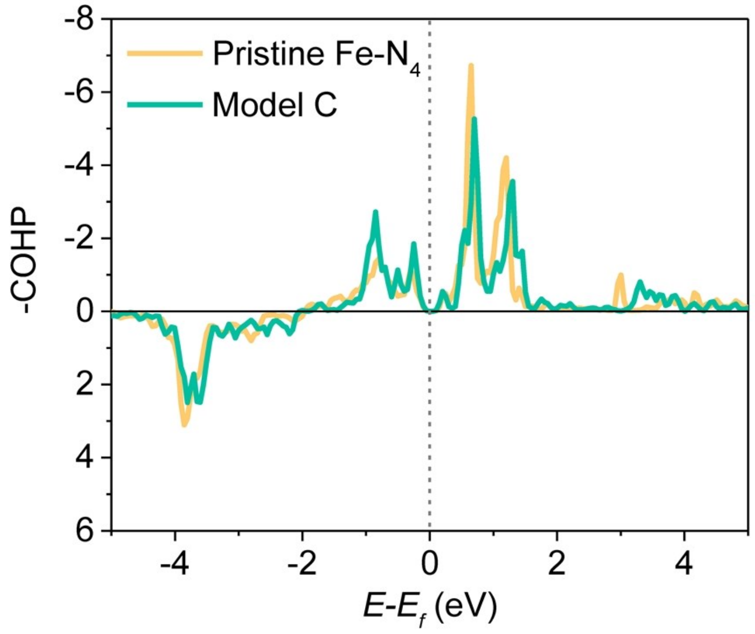

Figure S10. Crystal orbital Hamilton population (COHP) analysis of Fe-O bond for the pristine Fe-N$_4$ and model C sites.

References

1 D. Xia, X. Yang, L. Xie, Y. Wei, W. Jiang, M. Dou, X. Li, J. Li, L. Gan and F. Kang, *Adv. Funct. Mater.*, 2019, **29**, 1906174.

2 S. G. Ji, H. Kim, C. Park, W. Kim and C. H. Choi, *ACS Catal.*, 2020, **10**, 10773-10783.

3 D. Malko, A. Kucernak and T. Lopes, *Nat. Commun.*, 2016, **7**, 13285.

4 X. Wan, X. Liu, Y. Li, R. Yu, L. Zheng, W. Yan, H. Wang, M. Xu and J. Shui, *Nat. Catal.*, 2019, **2**, 259-268.

5 L. D. Pan, L. Z. Zhang, B. Q. Song, S. X. Du and H. J. Gao, *Appl. Phys. Lett.*, 2011, **98**, 666.

6 G. K. A and J. F. b, *Comput. Mater. Sci.*, 1996, **6**, 15-50.

7 G. Kresse and D. Joubert, *Phys. Rev. B*, 1999, **59**, 1758-1775.

8 J. P. Perdew, K. Burke and M. Ernzerhof, *Phys. Rev. Lett.*, 1996, **77**, 3865-3868.

9 J. K. N?Rskov, J. Rossmeisl, A. Logadottir, L. Lindqvist, J. R. Kitchin, T. Bligaard and H. Jónsson, *J. Phys. Chem. B*, 2004, **108**, 17886-17892.

10 V. L. Deringer, A. L. Tchougreeff and R. Dronskowski, *J. Phys. Chem. A*, 2011, **115**, 5461-5466.

11 S. Maintz, V. L. Deringer, A. L. Tchougreeff and R. Dronskowski, *J. Comput. Chem.*, 2016, **37**, 1030-1035.